

CrystEngComm

Accepted Manuscript



This is an *Accepted Manuscript*, which has been through the Royal Society of Chemistry peer review process and has been accepted for publication.

Accepted Manuscripts are published online shortly after acceptance, before technical editing, formatting and proof reading. Using this free service, authors can make their results available to the community, in citable form, before we publish the edited article. We will replace this *Accepted Manuscript* with the edited and formatted *Advance Article* as soon as it is available.

You can find more information about *Accepted Manuscripts* in the [Information for Authors](#).

Please note that technical editing may introduce minor changes to the text and/or graphics, which may alter content. The journal's standard [Terms & Conditions](#) and the [Ethical guidelines](#) still apply. In no event shall the Royal Society of Chemistry be held responsible for any errors or omissions in this *Accepted Manuscript* or any consequences arising from the use of any information it contains.

ARTICLE

Morphological and Orientational Diversity of LiFePO₄ Crystallites: Remarkable Reaction Path Dependence in Hydrothermal/Solvothermal Syntheses

Cite this: DOI: 10.1039/x0xx00000x

Zhaojin Li,^{a,b} Kongjun Zhu,^c Jialin Li,^a and Xiaohui Wang^{a,*}Received 00th January 2014,
Accepted 00th January 2014

DOI: 10.1039/x0xx00000x

www.rsc.org/

Abstract: We design four-group experiments to understand the morphological and orientational diversity of LiFePO₄ crystallites in hydrothermal and/or solvothermal syntheses. In the solvothermal synthesis in which water is highly deficient, the starting Li₃PO₄ nanoparticle likely directly evolves into LiFePO₄ through an in situ transition mechanism. In contrast, under the other three conditions, i.e., hydrothermal synthesis with stoichiometric H₃PO₄, hydrothermal and solvothermal syntheses in the presence of excess H₃PO₄, the starting Li₃PO₄ nanoparticle undergoes three diverse paths, generating different precursors and/or intermediates whose compositions and dissolution properties remarkably diverge. Such divergence in reaction paths dramatically influence the colloidal stability of the small, primary nanosheets participating in oriented-attachment aggregation growth, resulting in the diversity of the resultant LiFePO₄ in crystallite size from nanometer to micrometer and shape (rod-like platelet, slab, and flake), orientation ([010], [100] and [211]) and point defect concentration as well. Electrochemical performances of the diverse LiFePO₄ crystallites synthesized in this study correlate well with the morphological and orientational diversity, shedding light on tailored synthesis of LiFePO₄ crystallites for high-performance lithium-ion batteries.

1 Introduction

Since its electrochemical activity was reported by Padhi *et al.* in 1997, olivine-structured lithium iron phosphate LiFePO₄ (LFP), as a cathode material for lithium-ion batteries (LIBs), has attracted intensive attentions.¹ Due to being inexpensive and environmental benignity, covalently bonded PO₄ groups together with the chemically more stable Fe²⁺/Fe³⁺ couple offering excellent thermal stability and long duration safety,^{1,2} LFP is superior over other cathode materials such as LiCoO₂ and LiMn₂O₄.

On the other hand, high requirements on morphology and orientation control for achieving desired performances are raised for LFP due to its low electronic conductivity and sluggish lithium ion diffusion.³ The commercial success of new cathode materials mainly depends on the preparation methods in a controlled manner. Many synthetic strategies, including solid state reactions,¹ co-precipitation,^{4,5} sol-gel routes,^{6,7} and hydrothermal/solvothermal syntheses,⁸⁻¹⁵ have been therefore proposed to develop LFP particles. Among those methods, hydrothermal/solvothermal syntheses take advantages of low temperature, environmental benign, and low cost as well.¹⁶ Additionally, in the typical hydrothermal/solvothermal syntheses of LFP particles, the ferric source of LFP is FeSO₄·7H₂O. This sulfate is usually regarded as a useless byproduct generated during the industrial production of TiO₂. Million tons of FeSO₄·7H₂O is produced per year in the world. Thus, employing hydrothermal/solvothermal syntheses of LFP

particles could use up the byproduct of FeSO₄·7H₂O that has been treated as an environment waste.

Generally, the formation of LFP during hydrothermal/solvothermal syntheses involves a heterogeneous nucleation, namely dissolution-recrystallization process,¹⁷⁻²⁰ while nucleation and crystallite growth greatly depend on a wealth of factors including solvent, concentration, temperature, duration and pH *et al.*^{17,21,22} Therefore, much efforts have been devoted to study the roles of the factors in synthesizing LFP. For instance, Ellis *et al.*¹⁷ reported that increasing reactant concentration strongly favors the formation of nanocrystalline products. Dokko *et al.*²¹ stated that the particle morphology, crystallite orientation, and electrochemical reactivity of the prepared LFP particles changed depending on the concentration of the Li source and pH of the precursor. Wang *et al.*²² synthesized nano-sized LFP particles through varying concentration of starting materials, pH, process duration and temperature. Alternatively, researchers have made efforts to control the particle morphology, crystallite orientation and electrochemical performance by adopting various solvents including benzyl alcohol,^{13,23} ethylene glycol (EG),^{12,15,24-27} triethylene glycol,²⁸ tetraethylene glycol,^{29,30} and poly(ethylene glycol).³¹⁻³³ For instance, Zhu *et al.* reported the synthesis and nanostructural development of polycrystalline and single crystalline LFP nanostructures using tri(ethylene glycol) as a medium.³⁴ In this sense, solvents are very crucial due to their multiple roles during the solvothermal process. Very recently, Wang *et al.*³⁵ successfully obtained LFP nanoplates with crystal

orientation along the *ac* facet through adding excess H_3PO_4 in the solvothermal reaction system. The prepared LFP nanoplates exhibited excellent performance at high charge/discharge rates. It is well acknowledged that the electrochemical performance of synthesized LFP particulates is morphology and orientation dependent. However, knowledge concerning the morphological and orientational diversity is insufficient, and in-depth investigation of the underlying mechanism for the diversity of LFP crystallites is therefore required.

In this paper, we design four-group experiments using anhydrous Li_3PO_4 nanoparticles as the starting material to understand morphological and orientational diversity of LFP crystallites synthesized hydrothermally/solvothermally. The starting Li_3PO_4 nanoparticle undergoes four diverse paths, generating different precursors and/or intermediates whose compositions and dissolution properties remarkably diverge. Such divergence in reaction path dramatically influences the colloidal stability of the small, primary nanosheets participating in oriented-attachment aggregation growth, resulting in the morphological and orientational diversity of the synthesized LFP crystallites. The diversity of resultant LFP crystallites is attributed to the solution circumstance in which the molar ratios of the ions released from the various precursors/intermediates are different. Electrochemical performances of the diverse LFP crystallites synthesized in this study correlate well with the morphological and orientational diversity, shedding light on tailored synthesis of LFP crystallites for high-performance LIBs.

2 Experimental details

All chemicals (AR grade) used in this study were purchased from Sinopharm Chemical Reagent. They were used as received without any further purification. The water content in the EG is less than 0.1% as declared by the manufacturer.

2.1 Synthesis of anhydrous Li_3PO_4 powder

To investigate the influence of water on the formation of the precursors in the four-group experiments, anhydrous Li_3PO_4 powder was used as starting material. The Li_3PO_4 nanopowder was prepared by acid and alkali neutralization reaction of H_3PO_4 and LiOH . Briefly, lithium hydroxide solution (0.5 M) was prepared by dissolving $\text{LiOH}\cdot\text{H}_2\text{O}$ in deionized water. H_3PO_4 (85% solution) was subsequently added drop wise within 5 minutes into the solution under magnetic stirring and a white suspension formed. After magnetic stirring at room temperature for another 15 minutes, the resulting suspension was filtered using a porous membrane filter (0.22 μm pore size), washed several times with deionized water, and finally dried at 110 $^\circ\text{C}$ for 12 h. Then the obtained Li_3PO_4 was sealed in a resealable plastic bag and stored in a desiccator for further experiments.

2.2 Preparation of LiFePO_4 precursors and intermediates

To study the effects of H_2O and excess H_3PO_4 (EP) on the precursors, four types of precursors were designed and obtained. These four LFP precursors were prepared by either hydrothermal (H) or solvothermal (S) method using the afore-prepared Li_3PO_4 nanopowder, H_3PO_4 (85% solution), and $\text{FeSO}_4\cdot 7\text{H}_2\text{O}$ as the starting materials. The precursors include H-UR (usual ratio in which the molar ratio of $\text{Li}:\text{Fe}:\text{P} = 3:1:1$), S-UR, H-EP, and S-EP. Details for the preparation of the four precursors are summarized in Table 1.

In a typical preparation of H-UR precursor, Li_3PO_4 (6.800 g) was added to a solution with equal volume (30 mL) of H_2O and EG in a 100 mL-capacity stainless steel autoclave under magnetic stirring at room temperature. $\text{FeSO}_4\cdot 7\text{H}_2\text{O}$ (0.06 mol) was subsequently added to the suspension to make the molar ratio of $\text{Li}:\text{Fe}:\text{P} = 3:1:1$. After stirring at room temperature for 30 minutes, the resulting suspension was filtered using a porous membrane filter (0.22 μm pore size), washed several times with the solvent having the same composition as the synthesizing solvent. Finally, it was dried in a vacuum desiccator at room temperature for 72 h to avoid oxidation of the precursor as much as possible.

The intermediates were synthesized in a similar way to the precursors. After adding raw materials, the autoclave was sealed and heated in a silicon oil bath up to a preset temperature without holding time (donated this sample as H-UR (temperature)), except for the S-UR (180) sample that was obtained by heating up to 180 $^\circ\text{C}$ and holding at that temperature for 30 minutes. For example, if the sample was heated up to 100 $^\circ\text{C}$, the as synthesized sample was donated as H-UR (100). To investigate the temperature accurately, the temperature in this study refers to the inner temperature (the temperature inside the autoclave) unless specified otherwise. The inner temperatures are indicated by a thermocouple that was immersed into the autoclave. The S-UR, H-EP, and S-EP samples were synthesized in the same way except that the H-EP and S-EP samples were synthesized by adding 2.0 mL of H_3PO_4 (85% solution) after adding 6.800 g of Li_3PO_4 , and the S-UR and S-EP samples were synthesized by only using 60 mL EG as solvent. Unlike the precursors, the resulting intermediate was dried at 60 $^\circ\text{C}$ for 12 h.

2.3 Fabrication of LiFePO_4 powders

LFP powders with different morphologies were prepared using the same method as preparing the above precursors. The H-UR, S-UR, H-EP, and S-EP samples were synthesized by heating up to 180 $^\circ\text{C}$ and holding at that temperature for 30 minutes (donated these samples as H-UR (LFP), S-UR (LFP), H-EP (LFP), and S-EP (LFP), respectively).

Table 1. Starting materials for preparing the precursors

Samples	H_2O	EG	Li_3PO_4	H_3PO_4 (85%)	$\text{FeSO}_4\cdot 7\text{H}_2\text{O}$	$\text{Li}:\text{Fe}:\text{P}$ (molar ratio)
H-UR	30 mL	30 mL	6.800 g	—	0.06 mol	3:1:1
S-UR	—	60 mL	6.800 g	—	0.06 mol	3:1:1
H-EP	30 mL	30 mL	6.800 g	2.0 mL	0.06 mol	3:1:1.5
S-EP	—	60 mL	6.800 g	2.0 mL	0.06 mol	3:1:1.5

ARTICLE

2.4 Materials Characterization

Phase composition of the LFP powders, precursors, and those heated up to various temperatures were characterized by X-ray diffraction (XRD; Rigaku, D/max-2400) using Cu $K\alpha$ radiation. Fourier transform infrared spectra were recorded in a spectrometer (FTIR; PerkinElmer, Spectrum One) at room temperature. The unpolarized Raman spectra were collected on a Raman spectrometer (HORIBA Jobin Yvon, HR800). Simultaneous thermogravimetry and differential scanning analysis (TG/DSC; Setaram, Setsys 16–18) was conducted at a heating rate of 5 °C min⁻¹ under a high purity argon atmosphere. Inductively coupled plasma atomic emission spectrometer (ICP–AES; Thermo Elemental, IRIS Intrepid) was used to determine the chemical compositions of the intermediate phases. Morphological studies of the precursors and LFP powders were conducted by scanning electron microscopy (SEM; LEO, Super35). Brunauer–Emmett–Teller specific surface areas (BET; Micromeritics, ASAP 2020) were measured with nitrogen as adsorption gas at 77 K. A transmission electron microscope (TEM; FEI, Tecnai G2 F20),

operated at 200 kV, was used to identify crystallite size, morphology, and crystal orientation.

2.5 Electrochemical Performance

The as-synthesized LFP powders were firstly mixed with sucrose at a weight ratio of 1: 0.25, followed by heating up to 650 °C at a rate of 5 °C/min, and holding at that temperature for 3 h in an atmosphere of 95% Ar and 5% H₂ to obtain a LFP/C composite. The film electrodes prepared for electrochemical tests consisted of 80 wt% cathode composite, 10 wt% acetylene black as the conducting agent, and 10 wt% poly(vinylidene fluoride) as the binder. For comparison, the film electrodes consisting of 90 wt% carbon-coated LFP composite, 10 wt% poly(vinylidene fluoride), and those having 80 wt% bare LFP, 15 wt% acetylene black, and 5 wt% poly(vinylidene fluoride) were prepared. Pure metallic lithium was used as the anode. The electrolyte was 1 M LiPF₆ in ethylene carbonate/dimethyl carbonate/ethyl methyl carbonate solution (1:1:1 in volume). The assembled cells were galvanostatically cycled at various charge and discharge rates using a LAND CT2001A cyler (Wuhan Kingnuo Electronic Co., China) in the potential range of 2.3–4.2 V.

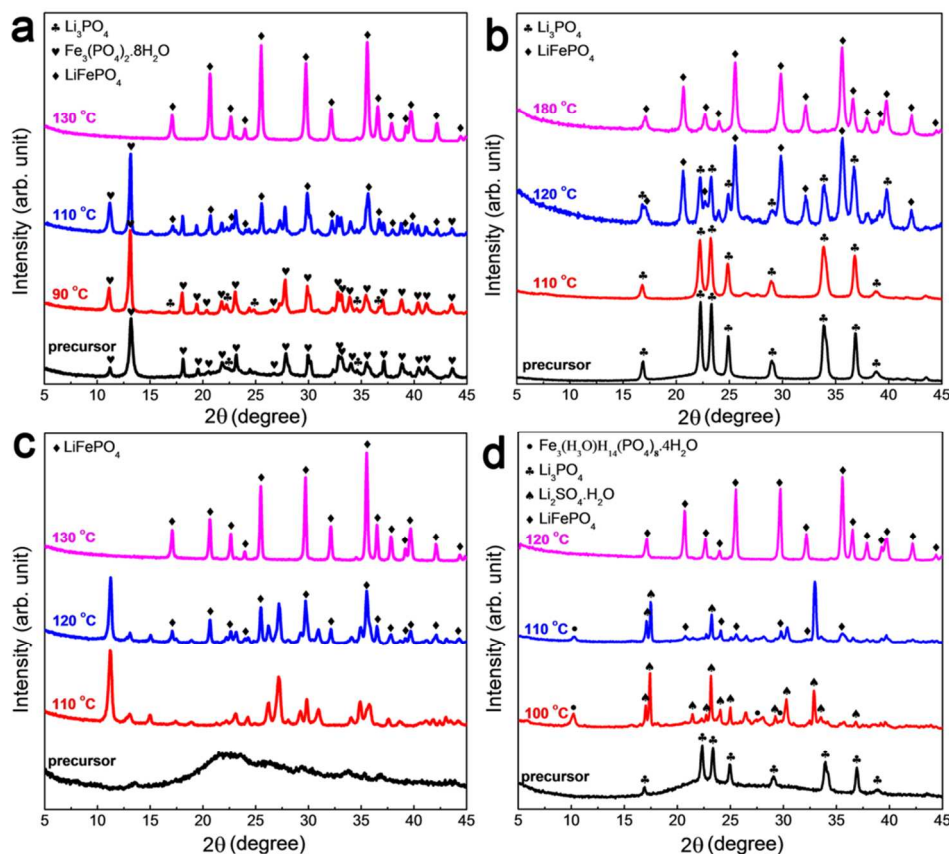


Fig. 1 XRD patterns of precursors and samples heated up to the temperatures indicated, showing phase evolution upon heating. (a) H–UR, (b) S–UR, (c) H–EP, and (d) S–EP.

ARTICLE

3 Results and discussion

3.1 Reaction path diversity concerning the solvent: Role of H₂O3.1.1 Reaction path in hydrothermal synthesis of LiFePO₄ with stoichiometric H₃PO₄

Hydrothermally prepared LFP powders are usually achieved by using LiOH, H₃PO₄ and FeSO₄·7H₂O with a molar ratio of Li:Fe:P = 3:1:1 as raw materials as described in the literature^{10,18,36}. In this study instead, anhydrous Li₃PO₄ was used as the source of lithium cation and phosphate anion. Fig. 1a shows the XRD patterns of the precursor and those heated up to various temperatures, from which we can see that the precursor consists of predominant Fe₃(PO₄)₂·8H₂O (JCPDS No. 30–0662) and minor Li₃PO₄ (JCPDS No. 25–1030). In spite of different sources of lithium cation and phosphate anion, the same resultant Fe₃(PO₄)₂·8H₂O was always yielded. This result indicates that this compound under such hydrothermal conditions is much more stable than Li₃PO₄ although the latter alone has low solubility in water. No other phases but

Fe₃(PO₄)₂·8H₂O and Li₃PO₄ are identified for the samples heated up to 90 °C. As the inner temperature increases up to 110 °C, the formation of target phase LFP (JCPDS No. 40–1499) is identified. It is noted that the space group notation for LFP is Pnmb in the database, while another notation of Pnma is widely adopted by the community. For this reason, we adopt the latter notation for LFP in this study unless specified otherwise. Phase-pure LFP is obtained as soon as the temperature reaches 130 °C.

In accordance with the XRD results, FTIR data (Fig. 2a) also identify the evolution from Fe₃(PO₄)₂·8H₂O to LFP. Upon heating, the ν_1 and ν_3 modes centered at 939 cm⁻¹ and 1044 cm⁻¹ which are assigned respectively to the symmetric and asymmetric vibration of P–O in PO₄³⁻ units³⁷ of Fe₃(PO₄)₂·8H₂O decline. Meanwhile, the ν_4 mode at 633 cm⁻¹ corresponding to the asymmetric bending of O–P–O in PO₄³⁻ units³⁷ of LFP strengthens. These experimental evidences indicate the formation of LFP at the expense of Fe₃(PO₄)₂·8H₂O.

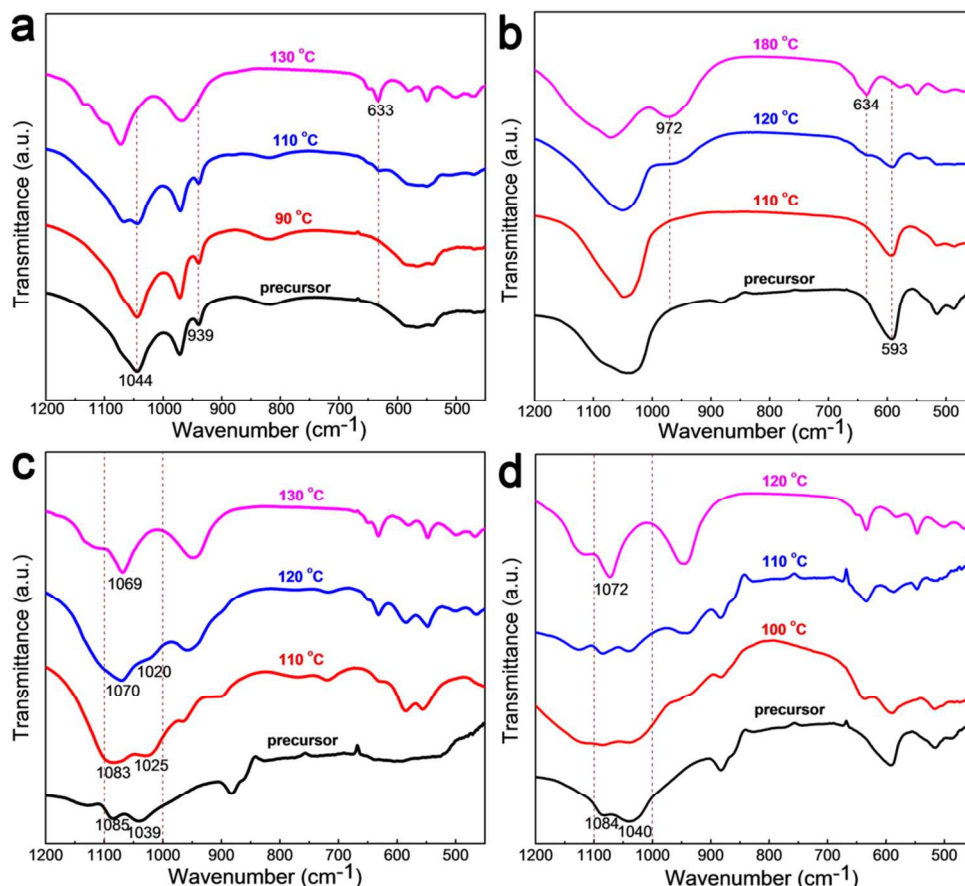


Fig. 2 FTIR patterns of the samples prepared under four different conditions. (a) H–UR, (b) S–UR, (c) H–EP, and (d) S–EP.

ARTICLE

3.1.2 Reaction path in solvothermal synthesis of LiFePO₄ with stoichiometric H₃PO₄

To study the path dependence in solvothermal synthesis of LFP, anhydrous EG was used to replace H₂O as the solvent to create a condition as waterless as possible. Fig. 1b presents the XRD patterns of S-UR (precursor) and those heated up to various temperatures, from which we can see that the precursor consists of Li₃PO₄ (JCPDS No. 25–1030). As the inner temperature increases to 120 °C, LFP is identified. Phase pure LFP is not obtained until the inner temperature reaches 180 °C and holds at that temperature for 30 minutes. A striking difference between hydrothermal synthesis (H-UR) and solvothermal synthesis (S-UR) in this study is that the reaction paths are quite different. In the H-UR, the intermediate phase is Fe₃(PO₄)₂·8H₂O. Whereas, LFP is most likely to undergo an in situ evolution from the starting material of Li₃PO₄.

In support of the in situ transformation, FTIR spectra are plotted in Fig. 2b. The 593 cm⁻¹ absorption band that is assigned to the asymmetric vibration of O–P–O (V_4) in PO₄³⁻ units³⁷ of Li₃PO₄, weakens gradually, while the absorption bands at 972 cm⁻¹ and 634 cm⁻¹ respectively corresponding to the symmetric stretching vibration of P–O and asymmetric bending of O–P–O in PO₄³⁻ units^{37,38} of LFP, get stronger and stronger.

Moreover, the in situ transformation from Li₃PO₄ to LFP is also witnessed by Raman spectroscopy that is a surface- and structure-sensitive analysis technique. (Fig. S1, Supporting Information). For the starting material, three distinct Raman bands located at 944, 1022, and 1064 cm⁻¹, in the range of 900 and 1100 cm⁻¹, correspond to symmetric stretching vibration of P–O and asymmetric bending of O–P–O in PO₄³⁻ units of Li₃PO₄, respectively.^{38,39} In the case of the final product, the bands at 951, 985, and 1071 cm⁻¹, are assigned to symmetric stretching vibration of P–O and asymmetric bending of O–P–O in PO₄³⁻ units of LFP, respectively.^{38,39} Whereas, for the intermediate sample heated up to 120 °C, the spectrum exhibits the characteristic bands of both Li₃PO₄ and LFP. In addition, a profound background is identified for the sample S-UR (110), indicating the circumstance of the PO₄ tetrahedra becomes disordered. In other words, an amorphization process involving the collapse of PO₄³⁻ units, i.e., the skeleton of Li₃PO₄, occurred during the transformation from Li₃PO₄ to LFP. In combination with the XRD, FTIR and Raman results, it is reasonable to state that the formation of S-UR (LFP) is achieved by in situ transformation from Li₃PO₄ to LFP via an amorphization process. The possible crystallite structure transformation diagrams are illustrated in Fig. S2 (Supporting Information). As is address in the following section, the morphology of LFP keeps the same as the starting Li₃PO₄, which further supports the speculation of the in situ transition.

3.1.3 Role of H₂O in the reaction path diversity in hydrothermal/solvothermal syntheses of LiFePO₄

By comparing phase evolution involved in the former two groups of experiments (H-UR and S-UR), it is clear that H₂O

significantly promotes the formation of LFP. The main contribution of H₂O is that it is a strong polar solvent, which facilitates the dissolution of Li₃PO₄ and the intermediate phase Fe₃(PO₄)₂·8H₂O. In contrast, EG under the solvothermal condition is not likely able to dissociate the starting material Li₃PO₄ into lithium cations and phosphate anions.

To further understand the reaction paths under other anhydrous conditions, EG was replaced by other solvents including ethanol, glycerol and polyethylene glycol 200. In these solvents, no other phases but Li₃PO₄ and LFP are identified in the samples heated up to 120 °C (Fig. S3), indicating in situ transformation from Li₃PO₄ to LFP. This is the same as the condition under which EG is used as solvent.

3.2 Reaction path diversity concerning the raw materials: Role of excess H₃PO₄**3.2.1 Reaction path in hydrothermal synthesis of LiFePO₄ with excess H₃PO₄**

To understand the effect of excess H₃PO₄, H₃PO₄(85%) was excessively added to the hydrothermal synthesis system. Upon introducing additional H₃PO₄, the precursor appeared to be amorphous. Interestingly, an intermediate phase is identified upon heating, as shown in Fig. 1c. This intermediate phase is quite different from Fe₃(PO₄)₂·8H₂O formed under the H-UR condition according to the XRD results. In addition to the difference in XRD patterns, the intermediate phase has a specific FTIR spectrum (Fig. 2c). Between 1100 cm⁻¹ and 1000 cm⁻¹, there are two absorption bands located at 1085 cm⁻¹ and 1039 cm⁻¹ in the H-EP (precursor). These two V_3 modes are regarded as the asymmetric vibration of P–O in PO₄³⁻ and HPO₄²⁻ units,^{37,40} respectively. With the increase in temperature, the asymmetric vibration in PO₄³⁻ shifts to a low wave number, and finally located at 1069 cm⁻¹ when pure phase LFP is obtained. Meanwhile, the absorption band at 1039 cm⁻¹ becomes weaker and weaker till disappears. Thus far, this intermediate phase has not been well understood. We therefore investigated the H-EP (110) sample by means of simultaneous TG/DSC and chemical analysis.

To gain insight into the structure of the H-EP (110), it was subjected to TG/DSC thermal analysis. Weight loss is obvious upon heating at temperature above 150 °C. So we speculate that the H-EP (110) sample (intermediate) contains crystal water. A strong exothermic peak at 488 °C is observed (Fig. 3a), suggesting a crystallization process. Fig. 3b shows the XRD patterns of the H-EP (110) sample, and those heated at 420 and 550 °C. For the sample heated at 420 °C, it exhibits an amorphous feature. Upon heating, crystal water in the H-EP (110) gives off from the skeleton and the structure collapses, forming an amorphous structure. At elevated temperature, recrystallization of LFP occurred.

Fig. 3c shows the TG/DSC curves of H-UR (90) sample. The endothermic peak at 120 °C attributes to the loss of free water, and peaks at 150 °C and 240 °C correspond to crystal water combining with Fe²⁺ and PO₄³⁻, respectively. Unlike the H-UR (90) sample which has two peaks at 150 °C and 240 °C, the H-

EP (110) exhibits a wider peak between 175 °C and 244 °C. This is because the bonding between Fe^{2+} and crystal water gets stronger in that kind of compound containing H^+ .

The H-EP (110) sample (intermediate) is subjected to inductive coupled plasma (ICP) analysis, demonstrating that the molar ratio of Li:Fe:P is 1:1.74:1.80, approximately equal to 4:7:7. As the states of Li, Fe, and P in LiFePO_4 are Li^+ , Fe^{2+} and PO_4^{3-} , respectively. For charge balance, excess of H^+ should therefore be involved into the intermediate, considering the excess H_3PO_4 in the reaction system. The intermediate phase, H-EP (110) has a nominal chemical formula of $\text{Fe}_7\text{H}_x\text{Li}_4(\text{PO}_4)_{7.7}\text{H}_2\text{O}$.

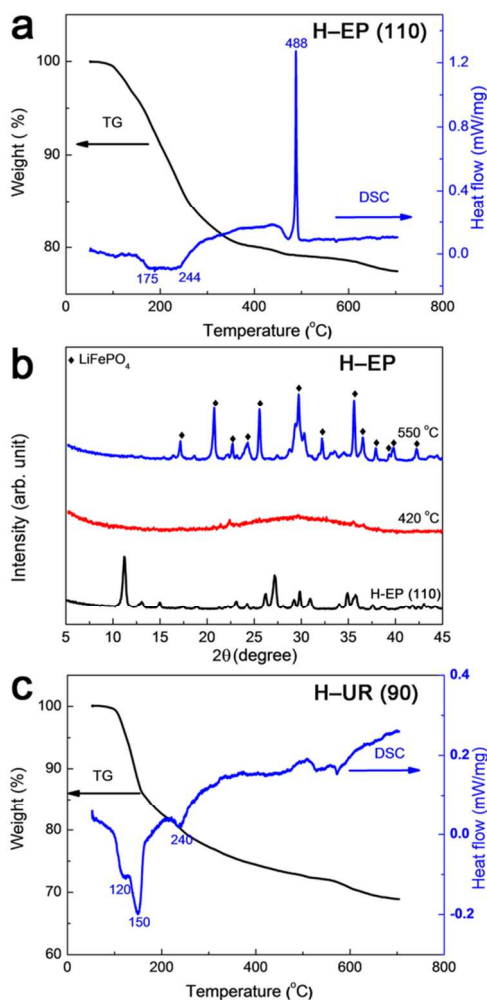


Fig. 3 Characterization of the intermediates of H-EP sample and H-UR sample. (a) simultaneous TG/DSC of H-EP (110), (b) XRD patterns of the H-EP sample treated at different temperatures in Ar, and (c) TG/DSC of H-UR (90).

3.2.2 Reaction path in solvothermal synthesis of LiFePO_4 with excess H_3PO_4

When pure EG was used as the solvent, from the XRD patterns in Fig. 1d, we can see the precursor mainly consists of Li_3PO_4 (JCPDS No. 25-1030) and amorphous phase. $\text{Li}_2\text{SO}_4 \cdot \text{H}_2\text{O}$ (JCPDS No. 15-0873) and $\text{Fe}_3(\text{H}_3\text{O})\text{H}_{14}(\text{PO}_4)_8 \cdot \text{H}_2\text{O}$ (JCPDS No. 38-1440) are identified as the main phases from the XRD pattern at 100 °C (Fig. 1d). For the molecule of $\text{Fe}_3(\text{H}_3\text{O})\text{H}_{14}(\text{PO}_4)_8 \cdot \text{H}_2\text{O}$, the element of Fe exists in the state of

Fe^{3+} . This is possibly because Fe^{2+} in the intermediate was oxidized upon exposure to air during the process of drying. This implies that the Fe^{2+} -containing intermediate is unstable under ambient condition. Here, we use $\text{Fe}_3(\text{H}_3\text{O})\text{H}_{14}(\text{PO}_4)_8 \cdot \text{H}_2\text{O}$ -like phase to represent the accurate phase in the intermediate. As the temperature increases to 110 °C, the target phase LFP is identified. Phase-pure LFP is observed when the temperature reaches 120 °C. Unlike the S-UR environment, Li_3PO_4 is unstable under such acidic condition. With increasing temperature, Li_3PO_4 gets amorphous and reacts with excess H_3PO_4 and $\text{FeSO}_4 \cdot 7\text{H}_2\text{O}$ to form the more stable phases, $\text{Fe}_3(\text{H}_3\text{O})\text{H}_{14}(\text{PO}_4)_8 \cdot \text{H}_2\text{O}$ -like phase and $\text{Li}_2\text{SO}_4 \cdot \text{H}_2\text{O}$. Fig. 2d shows the FTIR spectrum of the S-HE samples. Similar to the absorption bands of H-EP, between 1100 cm^{-1} and 1000 cm^{-1} , there are two bands located at 1084 cm^{-1} and 1040 cm^{-1} in the S-EP (precursor), indicating the existence of PO_4^{3-} and HPO_4^{2-} units based on the above analysis. Upon heating, the asymmetric vibration in PO_4^{3-} shifts to a low wave number, and finally locates at 1072 cm^{-1} when pure phase LFP is obtained. Meanwhile, the intensity of the absorption band at 1040 cm^{-1} becomes weaker till disappear.

3.2.3 Role of excess H_3PO_4 in the reaction path diversity in hydrothermal/solvothermal syntheses of LiFePO_4

By analyzing the phase evolution in the last two groups of experiments (H-EP and S-EP), we believe that excess H_3PO_4 also promotes the formation of LFP. The main contribution of excess H_3PO_4 is rooted in the formation of H^+ -containing intermediate phase, which facilitates the formation of LFP.

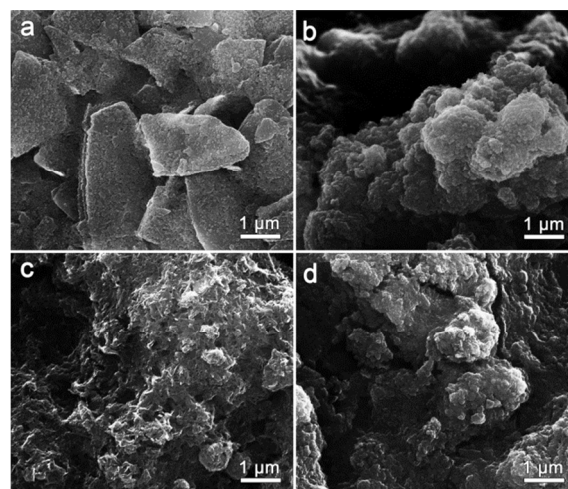


Fig. 4 SEM images of the precursors synthesized under different conditions. (a) H-UR (precursor), (b) S-UR (precursor), (c) H-EP (precursor), and (d) S-EP (precursor).

3.3 Morphology evolution and orientation determination under different hydrothermal and solvothermal conditions

Understanding the fundamental processes of crystallite growth, morphology evolution and crystallite orientation is of importance, as many of the properties are highly shape-, size- and orientation-dependent. Therefore, morphological studies by SEM and TEM are conducted.

Fig. 4–6 depict the SEM images of the precursors, intermediates and LFP synthesized under different hydrothermal and solvothermal conditions. Significant changes in morphology occur for the samples under the H-UR, H-EP

and S-EP conditions, whereas no visible morphology changes are observed for the samples under the S-UR condition in which water is highly deficient.

Under the H-UR condition, the precursor (Fig. 4a) consisting of $\text{Fe}_3(\text{PO}_4)_2 \cdot 8\text{H}_2\text{O}$ and Li_3PO_4 dissolved upon heating, followed by the nucleation and crystallite growth of LFP. Considering the rapid nature for the growth of LFP crystallites, it is reasonable to point out that the LFP crystallites grow at the expense of the ions in the vicinity of the dissolving intermediate (Fig. 5a-c). With long duration, the grains coarsen by aggregation, forming rod-like platelet shaped crystallites (Fig. 6a and 7a). By calculating the adsorption volume of nitrogen, the BET specific surface area of the H-UR (LFP) was determined to be $17.6 \text{ m}^2 \text{ g}^{-1}$. In consistent with the previous theoretical calculations in which the surface energy of the (010) planes is the smallest⁴¹, the LFP crystals formed under the H-UR condition are [010] oriented, as shown in the selected area electron diffraction (SAED) pattern (Fig. 7a).

Under the S-UR condition in which there is much less water, the S-UR (LFP) has to be evolved directly from Li_3PO_4 . From the images of SEM and TEM (Fig. 4b, 6b and 7b) we can see the precursor and S-UR (LFP) depict a similar morphology. Both of them consist of ultra-fine flakelets (about 20 nm) in aggregation. The BET specific surface area of the S-UR (LFP) was determined to be $19.2 \text{ m}^2 \text{ g}^{-1}$. Furthermore, the SEM images of S-UR (temperature) samples show a similar morphology (Fig. 5d-f). These similar morphologies further prove that the synthesis of S-UR (LFP) follows the in situ reaction mechanism.

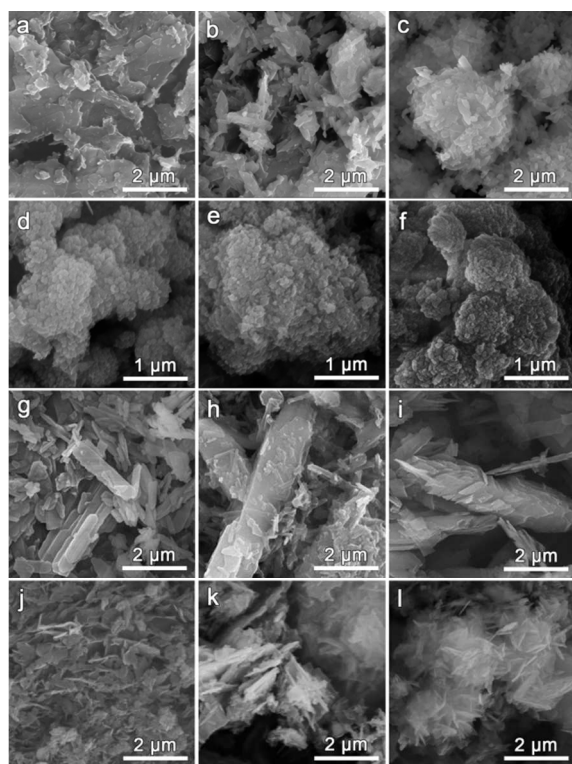


Fig. 5 Morphology evolution upon heating up to various temperatures under four synthetic conditions. H-UR (a-c), at 90 °C (a), 110 °C (b), and 130 °C (c). S-UR (d-f), at 110 °C (d), 120 °C (e), and 180 °C (f). H-EP (g-i), at 110 °C (g), 120 °C (h), and 130 °C (i). S-EP (j-l), at 100 °C (j), 110 °C (k), and 120 °C (l).

Under the H-EP condition where excess H_3PO_4 is involved, the initial agglomerated precursor consists of plenty of tiny needles (Fig. 4c). An intermediate phase with strip morphology (Fig. 5g) is formed as a result of the dissolution of the precursor in an amorphous state (Fig. 1c). Generally, the crystallite growth is described by aggregation at early times and high temperatures while by Ostwald ripening at later stages.⁴² Upon heating, the big strip intermediate aggregate dissolves, and LFP crystallite nucleus form and grow into slab-shaped LFP grains (Fig. 5h-i). Along with the increase in temperature, the LFP grains grow together into big slab-like morphology, with a length of about 5 μm and a width of about 1 μm (Fig. 6c). Due to large crystallite size, the BET specific surface area of the H-EP (LFP) is relatively low ($8.0 \text{ m}^2 \text{ g}^{-1}$). As shown in Fig. 7c, the big LFP slab shows an obvious contrast differences, indicating it is made up of small pieces. This is consistent with the theory where grains coarsen preferentially by aggregation in form of the oriented attachment.⁴³⁻⁴⁵ As indicated by the SAED pattern, the grains are [100] orientated.

Under the S-EP condition, the precursor is comprised of agglomerated small particles (Fig. 4d). From the XRD patterns (Fig. 1d) and the morphology of Li_3PO_4 (Fig. 4b), it is reasonable to conclude that the small particles are Li_3PO_4 that hasn't been dissolved. After a dissolution-recrystallization process, the intermediates ($\text{Fe}_3(\text{H}_3\text{O})\text{H}_{14}(\text{PO}_4)_8 \cdot \text{H}_2\text{O}$ -like phase and $\text{Li}_2\text{SO}_4 \cdot \text{H}_2\text{O}$) with an interlaced flake morphology are produced (Fig. 5j). The distinction in phase component and morphology between the S-EP (intermediate) and the H-EP (intermediate) is caused by the different solution composition and interfacial tension, for growth rates are controlled by solution composition^{46,47}, and interfacial tension⁴⁸. At the expense of intermediates dissolution, LFP nucleuses form and grow up attaching to the intermediates (Fig. 5k-l). Correspondingly, the harvested S-EP (LFP) crystallites present similar interlaced flake morphology to the intermediate (Fig. 6d). Due to a smaller crystallite size than the H-EP (LFP), the S-EP (LFP) has a larger specific surface area of $14.2 \text{ m}^2 \text{ g}^{-1}$.

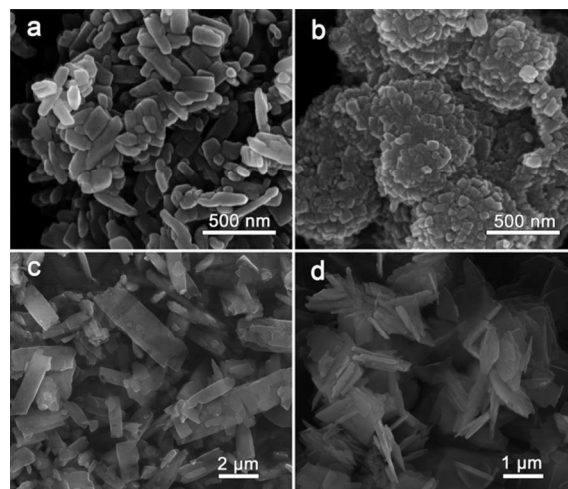


Fig. 6 SEM images of the LFP particles harvested after holding at 180 °C for 30 minutes under four different synthetic conditions, showing reaction path-dependent morphology. (a) rods (platelets) in hydrothermal synthesis (H-UR (LFP)), (b) flakelets of aggregation in solvothermal synthesis (S-UR (LFP)), (c) slabs in hydrothermal synthesis in the presence of H_3PO_4 (H-EP (LFP)), and (d) interlaced flakes in solvothermal synthesis in the presence of H_3PO_4 (S-EP (LFP)).

Similar to the H-EP (LFP), the S-EP (LFP) follows aggregation growth. According to the proposal by Wang and coworkers⁴⁹, where aggregation growth and Ostwald ripening are distinguished by nanoparticle core structure. As shown in Fig. 7d, the interlaced flake LFP “crystallites” also show obvious contrast differences, indicating they should be initially polycrystalline. Orientation determination demonstrates that [211] is the predominant orientation (Fig. 7d). To the best of our knowledge, this is the first time of being observed in the LFP crystallites. Besides the frequently observed [211] orientation, [100] orientation is occasionally observed. The coexistence of these two orientations witnesses a competition between them during the crystallites nucleation process.

Under the H-UR, H-EP and S-EP conditions, the growth of LFP crystallites follow the oriented attachment mechanism, but there is a dramatic diversity in crystallite size and shape, and orientation. This may be understood from the complexity of the three reaction systems. As was put forward by Wang et al.⁴⁹, the height (maximum nucleation rate) and width (2σ) of the nucleation function profile are systematically varied by conditions that influence the colloidal stability of the small, primary nanocrystallites participating in aggregative growth. Concerning that the growing up of LFP is closely associated with the dissolution of the intermediates, the diversity in this study is reasonably ascribed to the distinct solution circumstances caused by the different molar ratios of the ions released from the intermediates.

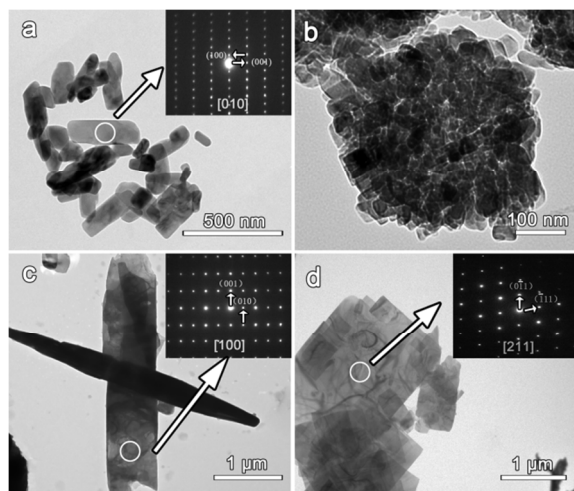


Fig. 7 TEM images of the LFP harvested after holding at 180 °C for 30 minutes under different conditions. (a) H-UR (LFP), (b) S-UR (LFP), (c) H-EP (LFP), and (d) S-EP (LFP). Insets show the corresponding SAED patterns.

3.4 Correlation between reaction path and concentration of antisite defect

It has been acknowledged that the Li ion migration in LFP is determined not only by crystallite size and diffusion pathway but also by the concentration of Fe_{Li} antisite defect, and Fe_{Li} defect in which Li sites are occupied by ferrous Fe^{2+} ions.^{50,51} According to the previous report,²⁰ the point defect concentration is closely linked to the symmetric stretching P-O vibration band of the PO_4 tetrahedron at 957 cm^{-1} . The red shift of this infrared absorption band represents a reduction in the point defect concentration. Fig. 8 shows the symmetric stretching P-O vibration bands of LFP that synthesized under

different conditions. As we can see, the symmetric stretching P-O vibration peak is around 970 cm^{-1} in the H-UR or S-UR (LFP) samples. While in the H-EP (LFP) or S-EP (LFP) samples, the symmetric stretching P-O vibration bands are significantly shifted to low wave numbers. The difference in their corresponding reaction paths may contribute to such remarkable difference in the symmetric stretching P-O vibration band of the PO_4 tetrahedron.

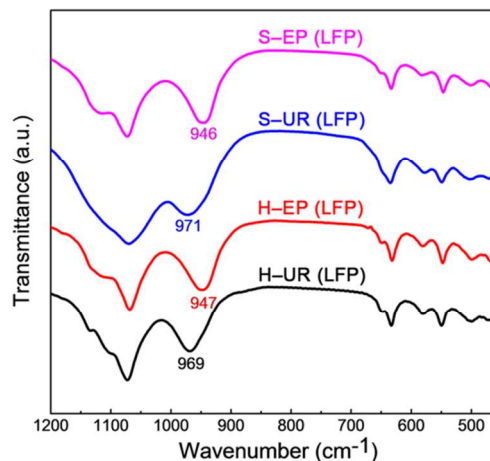


Fig. 8 FTIR spectra of the LFP harvested after holding at 180 °C for 30 minutes under different conditions.

Based on the afore-mentioned results of phase evolution and morphology change, and discussion as well, the formation of LFP follows a dissolution-precipitation mechanism under the conditions of H-UR, H-EP and S-EP. The LFP nucleuses grow up at the expense of the surrounding cations and anions.

For the H-UR (LFP), it evolved from the $\text{Fe}_3(\text{PO}_4)_2 \cdot 8\text{H}_2\text{O}$ intermediate phase. The crystallite nucleus formed and grew up attaching to the $\text{Fe}_3(\text{PO}_4)_2 \cdot 8\text{H}_2\text{O}$ intermediate phase. The surrounding solutes environment is that the concentration of Fe^{2+} is higher than PO_4^{3-} for it is mainly determined by the dissolution of the $\text{Fe}_3(\text{PO}_4)_2 \cdot 8\text{H}_2\text{O}$ intermediate. Defects of Fe_{Li} would easily form due to the excess Fe^{2+} in the vicinity of LFP crystallite nucleus. In contrast, in the presence of excess H_3PO_4 under the conditions of H-EP and S-EP, the LFP crystallites are synthesized from intermediate phases containing H^+ . The solutes environments surrounding the LFP crystallite nucleus both hold a common feature that the concentration of Fe^{2+} is lower than PO_4^{3-} . Then a lower defect concentration can be obtained. As for the S-UR (LFP), it is evolved directly from the precursor of Li_3PO_4 , in such a way that Li^+ gradually was replaced by the Fe^{2+} . A high concentration of Fe_{Li} antisite defect is inevitably introduced by this way of transformation.

3.5 Electrochemical Performance

As discussed above, the reaction path dependent diversity in hydrothermally/solvothermally synthesized LFP crystallites has been verified. The diversity in crystallite size, aggregation state, crystallite orientation, and point defect concentration provides an opportunity to study the correlation between the diversity and electrochemical performance of the resultant LFP crystallites.

Because the as-prepared LFP powders have much low electronic conductivity, a good contact between the LFP crystallites and conducting agent (usually acetylene black) is

required to characterize their intrinsic electrochemical properties. It is however very hard to thoroughly mix them with acetylene black to achieve a nice contact between the LFP crystallites and acetylene black. As a result, the cathodes made by mixing the as-prepared LFP powders with ethylene black, show poor electrochemical properties (Fig. S4). With carbon coating, even in the absence of acetylene black, the electrochemical properties are significantly improved (Fig. S5), indicating that carbon coating is an efficient approach to good contact between the LFP crystallites and current collector. Further adding acetylene black, the electrochemical properties are the best among the three methods of preparing the cathodes. We believe that the last cathode preparation method is capable of exhibiting the electrochemical performances of the synthesized LFP crystallites. We therefore use the data collected from the samples with carbon coating and acetylene black.

It should be emphasized that the morphologies of the LFP crystallites with carbon coating might change at the treated temperature. To examine whether this is the case or not, morphological investigation on the carbon-coated samples was conducted. Fig. S6 shows their typical morphologies, from which we can see that the morphologies are reserved with carbon coating. We also investigated the carbon-coated samples by FTIR to indicate the point defect concentrations. As plotted in Fig. S7, the symmetric stretching P–O vibration bands of H–UR (LFP/C) and S–UR (LFP/C) samples still remain at higher

wavenumbers than H–EP (LFP/C) and S–EP (LFP/C) samples. These results demonstrate that the carbon-coated samples, i.e., H–UR (LFP/C) and S–UR (LFP/C), have higher point defect concentrations than their counterparts of H–EP (LFP/C) and S–EP (LFP/C).

The H–UR (LFP/C) sample has a specific discharge capacity as high as 160 mAh g^{-1} at 0.1 C ($1 \text{ C} = 170 \text{ mA g}^{-1}$), which is close to the theoretical capacity (170 mAh g^{-1}). Even at a high charge/discharge rate of 20 C , the capacity can still reach almost 100 mAh g^{-1} . Meanwhile, this sample also delivers excellent Coulombic efficiency (Fig. 9a). This result is consistent with the theoretical study, which predicts that LFP crystallite with the [010] orientation can improve the rate capability.^{52,53} In addition, the point defects like Fe_{Li} that are popular in LFP can provide more negative electron carriers. At moderate levels of such defects, the increased electron carriers, give rise to improved electrical conductivity.⁵⁴ In contrast, the S–UR (LFP/C) sample only exhibits a discharge capacity of less than 120 mAh g^{-1} at the low current of 0.1 C . When the C-rate increases to 20 C , it presents a rather low discharge capacity of about 42 mAh g^{-1} (Fig. 9b). This may be attributed to its excessively high Fe_{Li} defect concentration, which hinders the Li^+ migration. On the other hand, the in situ formed crystallites are so fine (20 nm) that serious aggregation occurred, giving rise to an increased migration path for lithium cations.

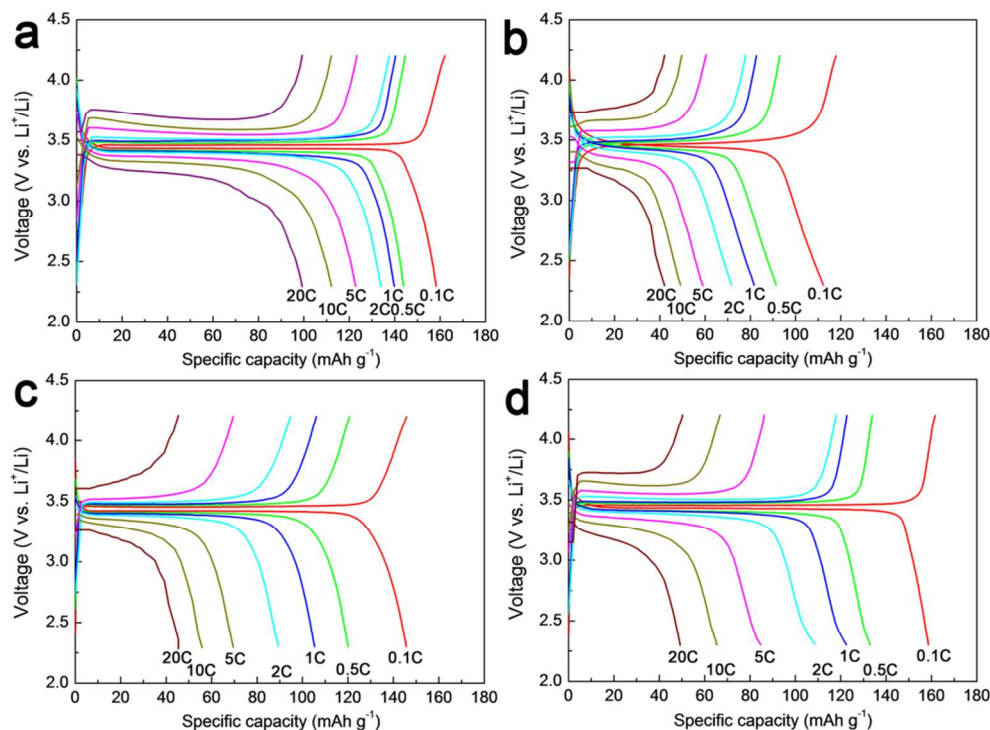


Fig. 9 Charge-discharge galvanostatic curves of (a) H–UR (LFP/C), (b) S–UR (LFP/C), (c) H–EP (LFP/C), and (d) S–EP (LFP/C).

Under the H_3PO_4 excess condition, the H–EP (LFP/C) sample presents a discharge capacity of 148 mAh g^{-1} at 0.1 C , while the S–EP (LFP/C) sample presents 160 mAh g^{-1} at 0.1 C . Both capacities are high considering their micrometer crystallite size. The low point defect concentration may contribute to the high capacities at low C-rate. Compared with

the H–UR (LFP/C), the H–EP (LFP/C) shows a faster drop on the discharge capacity as the increasing of C-rate. The H–EP (LFP/C) can only achieve a discharge capacity of 42 mAh g^{-1} at 20 C (Fig. 9c). This is caused not only by its big particle size but also by its [100] orientation, which is detrimental to the insertion and de-insertion of Li^+ ions. Similarly, the S–EP

(LFP/C) also presents a fast drop on the discharge capacity as the increasing of the C-rate, but shows a better performance than the H-EP (LFP/C). The S-EP (LFP/C) can present a discharge capacity of 50 mAh g⁻¹ at 20 C (Fig. 9d). The better performance is attributed to its smaller particle size⁵⁵⁻⁵⁸.

These results further witness that the electrochemical performance of LFP is decided by the integrated factors of the crystallite orientation,⁵⁹ crystallite size,⁵³ aggregation state,⁶⁰ and concentration of defect⁵². The knowledge established in this study sheds light on tailored synthesis of LiFePO₄ crystals for high-performance LIBs.

Conclusions

We have systematically investigated the reaction paths in hydrothermal/solvothermal syntheses of LFP, concerning the roles of H₂O and excess H₃PO₄. Both H₂O and excess H₃PO₄ are essential in promoting the synthesis of LFP. In the solvothermal synthesis, the starting anhydrous Li₃PO₄ nanopowder likely directly evolves into LFP through an in situ reaction mechanism. In contrast, under other three conditions, i.e., hydrothermal synthesis with stoichiometric H₃PO₄, hydrothermal and solvothermal syntheses in the presence of excess H₃PO₄, the starting Li₃PO₄ undergoes three diverse paths generating different precursors and/or intermediates. The precursors and/or intermediates are Fe₃(PO₄)₂·8H₂O in hydrothermal synthesis with stoichiometric H₃PO₄, Fe₇H₃Li₄(PO₄)₇·yH₂O in hydrothermal with excess H₃PO₄, and the mixture of Li₂SO₄·H₂O and Fe₃(H₃O)H₁₄(PO₄)₈·H₂O in solvothermal synthesis in the presence of excess H₃PO₄. The compositions and dissolution properties of those precursors and/or intermediates diverge remarkably. Such divergence in reaction paths dramatically influence the colloidal stability of the small, primary nanosheets participating in oriented-attachment aggregation growth, resulting in the diversity of the resultant LFP in grain size and shape, orientation and point defect concentration as well. The LFP with smaller size and thickness along the [010] direction shows superior electrochemical performance.

Acknowledgements

This work was supported by the Chinese Academy of Sciences (CAS) and the Institute of Metal Research, CAS.

Notes and references

^aShenyang National Laboratory for Materials Science, Institute of Metal Research, Chinese Academy of Sciences, 72 Wenhua Road, Shenyang 110016, China

^bUniversity of Chinese Academy of Sciences, Beijing 100039, China

^cState Key Laboratory of Mechanics and Control of Mechanical Structures, Nanjing University of Aeronautics and Astronautics, Nanjing 210016, China

*Address: E-mail: wang@imr.ac.cn. Phone: +86-24-83970549. Fax: +86-24-23891320.

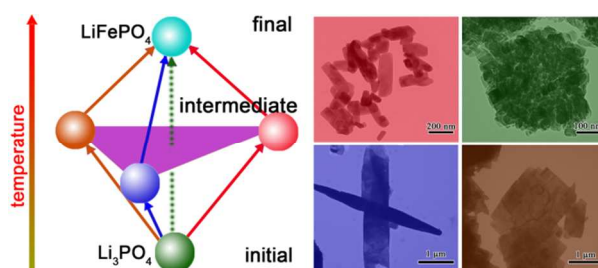
†Electronic Supplementary Information (ESI) available. See DOI: 10.1039/b000000x/

1 A. K. Padhi, K. S. Nanjundaswamy and J. B. Goodenough, *J. Electrochem. Soc.*, 1997, **144**, 1188-1194.

- 2 M. Koltypin, D. Aurbach, L. Nazar and B. Ellis, *Electrochem. Solid-State Lett.*, 2007, **10**, A40-A44.
- 3 L. X. Yuan, Z. H. Wang, W. X. Zhang, X. L. Hu, J. T. Chen, Y. H. Huang and J. B. Goodenough, *Energy Environ. Sci.*, 2011, **4**, 269-284.
- 4 G. Arnold, J. Garche, R. Hemmer, S. Strobele, C. Vogler and A. Wohlfahrt-Mehrens, *J. Power Sources*, 2003, **119**, 247-251.
- 5 S. Franger, F. Le Cras, C. Bourbon and H. Rouault, *J. Power Sources*, 2003, **119**, 252-257.
- 6 C. R. Sides, F. Croce, V. Y. Young, C. R. Martin and B. Scrosati, *Electrochem. Solid-State Lett.*, 2005, **8**, A484-A487.
- 7 D. Choi and P. N. Kumta, *J. Power Sources*, 2007, **163**, 1064-1069.
- 8 S. F. Yang, P. Y. Zavalij and M. S. Whittingham, *Electrochem. Commun.*, 2001, **3**, 505-508.
- 9 S. F. Yang, Y. N. Song, P. Y. Zavalij and M. S. Whittingham, *Electrochem. Commun.*, 2002, **4**, 239-244.
- 10 J. J. Chen and M. S. Whittingham, *Electrochem. Commun.*, 2006, **8**, 855-858.
- 11 G. Meligrana, C. Gerbaldi, A. Tuel, S. Bodoardo and N. Penazzi, *J. Power Sources*, 2006, **160**, 516-522.
- 12 K. Saravanan, M. V. Reddy, P. Balaya, H. Gong, B. V. R. Chowdari and J. J. Vittal, *J. Mater. Chem.*, 2009, **19**, 605-610.
- 13 H. Yang, X. L. Wu, M. H. Cao and Y. G. Guo, *J. Phys. Chem. C*, 2009, **113**, 3345-3351.
- 14 J. Qian, M. Zhou, Y. Cao, X. Ai and H. Yang, *J. Phys. Chem. C*, 2010, **114**, 3477-3482.
- 15 C. Sun, S. Rajasekhara, J. B. Goodenough and F. Zhou, *J. Am. Chem. Soc.*, 2011, **133**, 2132-2135.
- 16 M. K. Devaraju and I. Honma, *Adv. Energy Mater.*, 2012, **2**, 284-297.
- 17 B. Ellis, W. H. Kan, W. R. M. Makahnouk and L. F. Nazar, *J. Mater. Chem.*, 2007, **17**, 3248-3254.
- 18 X. Qin, X. Wang, H. Xiang, J. Xie, J. Li and Y. Zhou, *J. Phys. Chem. C*, 2010, **114**, 16806-16812.
- 19 J. Lim, J. Gim, S. W. Kang, S. Baek, H. Jeong and J. Kim, *J. Electrochem. Soc.*, 2012, **159**, A479-A484.
- 20 X. Qin, J. Wang, J. Xie, F. Li, L. Wen and X. Wang, *Phys. Chem. Chem. Phys.*, 2012, **14**, 2669-2677.
- 21 K. Dokko, S. Koizumi, H. Nakano and K. Kanamura, *J. Mater. Chem.*, 2007, **17**, 4803-4810.
- 22 L. Wang, W. Sun, X. Tang, X. Huang, X. He, J. Li, Q. Zhang, J. Gao, G. Tian and S. Fan, *J. Power Sources*, 2013, **244**, 94-100.
- 23 I. Bilecka, A. Hintennach, I. Djerdj, P. Novak and M. Niederberger, *J. Mater. Chem.*, 2009, **19**, 5125-5128.
- 24 C. Nan, J. Lu, C. Chen, Q. Peng and Y. Li, *J. Mater. Chem.*, 2011, **21**, 9994-9996.
- 25 L. Wang, F. Zhou, Y. S. Meng and G. Ceder, *Phys. Rev. B*, 2007, **76**, 165435.
- 26 K. Saravanan, P. Balaya, M. V. Reddy, B. V. R. Chowdari and J. J. Vittal, *Energy Environ. Sci.*, 2010, **3**, 457-464.
- 27 D. Rangappa, K. Sone, T. Kudo and I. Honma, *J. Power Sources*, 2010, **195**, 6167-6171.
- 28 J. S. Lim, D. H. Kim, V. Mathew, D. C. Ahn and J. K. Kim, *J. Nanosci. Nanotechnol.*, 2011, **11**, 1451-1454.
- 29 A. Vadivel Murugan, T. Muraliganth and A. Manthiram, *J. Phys. Chem. C*, 2008, **112**, 14665-14671.

- 30 A. Vadivel Murugan, T. Muraliganth and A. Manthiram, *Electrochem. Commun.*, 2008, **10**, 903-906.
- 31 A. Fedorkova, A. Nacher-Alejos, P. Gomez-Romero, R. Orinakova and D. Kaniansky, *Electrochim. Acta*, 2010, **55**, 943-947.
- 32 L. N. Wang, Z. G. Zhang and K. L. Zhang, *J. Power Sources*, 2007, **167**, 200-205.
- 33 Z. Xu, L. Xu, Q. Lai and X. Ji, *Mater. Res. Bull.*, 2007, **42**, 883-891.
- 34 J. Zhu, J. Fiore, D. Li, N. M. Kinsinger, Q. Wang, E. DiMasi, J. Guo and D. Kisailus, *Cryst. Growth Des.*, 2013, **13**, 4659-4666.
- 35 L. Wang, X. He, W. Sun, J. Wang, Y. Li and S. Fan, *Nano Lett.*, 2012, **12**, 5632-5636.
- 36 S. L. Yang, X. F. Zhou, J. G. Zhang and Z. P. Liu, *J. Mater. Chem.*, 2010, **20**, 8086-8091.
- 37 A. Ait Salah, P. Jozwiak, K. Zaghbi, J. Garbarczyk, F. Gendron, A. Mauger and C. M. Julien, *Spectrosc. Acta Pt. A-Molec. Biomolec. Spectr.*, 2006, **65**, 1007-1013.
- 38 C. M. Burba and R. Frech, *J. Electrochem. Soc.*, 2004, **151**, A1032-A1038.
- 39 W. Paraguassu, P. T. C. Freire, V. Lemos, S. M. Lala, L. A. Montoro and J. M. Rosolen, *J. Raman Spectrosc.*, 2005, **36**, 213-220.
- 40 C. Ben Hassen, M. Boujelbene and T. Mhiri, *J. Mol. Struct.*, 2013, **1049**, 36-40.
- 41 C. A. J. Fisher and M. S. Islam, *J. Mater. Chem.*, 2008, **18**, 1209-1215.
- 42 L. N. Schultz, K. Dideriksen, L. Lakshtanov, S. S. Hakim, D. Muter, F. Hausser, K. Bechgaard and S. L. S. Stipp, *Cryst. Growth Des.*, 2014, **14**, 552-558.
- 43 R. L. Penn, *Science*, 1998, **281**, 969-971.
- 44 R. L. Penn, *J. Phys. Chem. B*, 2004, **108**, 12707-12712.
- 45 C. Ribeiro, E. J. Lee, E. Longo and E. R. Leite, *Chemphyschem*, 2006, **7**, 664-670.
- 46 K. Larsen, K. Bechgaard and S. L. S. Stipp, *Geochim. Cosmochim. Acta*, 2010, **74**, 558-567.
- 47 K. Larsen, K. Bechgaard and S. L. S. Stipp, *Geochim. Cosmochim. Acta*, 2010, **74**, 2099-2109.
- 48 A. A. Chernov, *Usp. Fiz. Nauk*, 1961, **73**, 277-331.
- 49 F. Wang, V. N. Richards, S. P. Shields and W. E. Buhro, *Chem. Mater.*, 2014, **26**, 5-21.
- 50 R. Malik, D. Burch, M. Bazant and G. Ceder, *Nano letters*, 2010, **10**, 4123-4127.
- 51 P. Axmann, C. Stinner, M. Wohlfahrt-Mehrens, A. Mauger, F. Gendron and C. M. Julien, *Chem. Mater.*, 2009, **21**, 1636-1644.
- 52 M. Saiful Islam, D. J. Driscoll, C. A. J. Fisher and P. R. Slater, *Chem. Mater.*, 2005, **17**, 5085-5092.
- 53 S. Nishimura, G. Kobayashi, K. Ohoyama, R. Kanno, M. Yashima and A. Yamada, *Nat.Mater.*, 2008, **7**, 707-711.
- 54 F. Ye, L. Wang, X. He, M. Fang, Z. Dai, J. Wang, C. Huang, F. Lian, J. Wang, G. Tian and M. Ouyang, *J. Power Sources*, 2014, **253**, 143-149.
- 55 H. Huang, S. C. Yin and L. F. Nazar, *Electrochem. Solid-State Lett.*, 2001, **4**, A170-A172.
- 56 A. Yamada, S. C. Chung and K. Hinokuma, *J. Electrochem. Soc.*, 2001, **148**, A224-A229.
- 57 C. Delacourt, P. Poizot, S. Levasseur and C. Masquelier, *Electrochem. Solid-State Lett.*, 2006, **9**, A352-A355.
- 58 R. Malik, D. Burch, M. Bazant and G. Ceder, *Nano Lett.*, 2010, **10**, 4123-4127.
- 59 S. Ferrari, R. L. Lavall, D. Capsoni, E. Quartarone, A. Magistris, P. Mustarelli and P. Canton, *J. Phys. Chem. C*, 2010, **114**, 12598-12603.
- 60 H. Li, L. H. Shi, W. Lu, X. J. Huang and L. Q. Chen, *J. Electrochem. Soc.*, 2001, **148**, A915-A922.

For Table of Contents Use Only



Reaction path difference in synthesis conditions has resulted in the morphological and orientational diversity of resultant LiFePO_4 crystallites.